Delft University of Technology

Magnetic stray field measurements to identify and localise impact-induced plastic deformation in a steel structure

Meijers, P. C.; Jolink, C. T.; Tsouvalas, A.; Metrikine, A. V.

Citation (APA)
Meijers, P. C., Jolink, C. T., Tsouvalas, A., & Metrikine, A. V. (2022). Magnetic stray field measurements to identify and localise impact-induced plastic deformation in a steel structure. *International Journal of Mechanical Sciences*, *217*, Article 106990. https://doi.org/10.1016/j.ijmecsci.2021.106990

Important note
To cite this publication, please use the final published version (if applicable).
Please check the document version above.

Magnetic stray field measurements to identify and localise impact-induced plastic deformation in a steel structure

P.C. Meijers *, C.T. Jolink, A. Tsouvalas, A.V. Metrikine

Delft University of Technology, Faculty of Civil Engineering, Stevinweg 1, 2628CN Delft, The Netherlands

ARTICLE INFO

ABSTRACT

To study the irreversible changes in the magnetic stray field surrounding a steel structure caused by impact-induced elastic and plastic deformations, a steel cylinder was repeatedly subjected to axial impacts of various magnitudes. Due to impacts that induce elastic deformation, the measured magnetic stray field of the structure converges to a global magnetic equilibrium. However, as soon as plastic deformation develops, a deviation from this trend is observed. From the spatial distribution of the stray field, the location of the plastic deformation is determined. Subsequently, the underlying processes of the measured evolution of the stray field are discussed and successfully incorporated into an elementary model of the structure's magnetisation to simulate the results from the experiment. It is expected that the reported observation is useful for a class of engineering applications in which non-contact and non-collocated measurements can be utilised to identify structural damage under dynamic loading.

1. Introduction

Driven by the ambitious climate goals set out by governments to reduce the emission of greenhouse gasses, the demand for energy generated from renewable sources has soared during the past decade [1], and it is expected that this trend will continue in this new decade [2]. One attractive method to generate energy is the offshore wind turbine. Despite the plethora of available foundation types for such a structure, steel monopiles are the preferred choice in the relatively shallow North Sea [3]. Monopiles are thin-walled cylindrical structures with a diameter of several metres and a length of tens of metres, which are most commonly driven into the seabed by means of an hydraulic impact hammer. Each hammer blow generates a compressive stress wave, which propagates downwards along the pile and enables the pile's progression into the seabed. To overcome the increasing soil resistance at greater penetration depths, the input energy of the hammer is raised accordingly. Especially at the pile head, high-energy impacts may induce stresses close to the material's yield limit, increasing the risk of plastic deformations there.

Until recently, plastic deformations at the pile head were of little concern, as that part did not contribute significantly to the bearing capacity of the pile. However, the industry has switched to a new connection between the monopile and the superstructure that relies on a bolted flange connection [4]. This design change was necessary as undesired settlements of the previously-used grouted connections were registered [5,6]. A flanged connection has the additional benefit

that it reduces the total cost of wind turbine, as it requires less steel than the grouted version [7]. Nevertheless, the design does require a perfect alignment between the pile head and the superstructure. Any plastic deformation of the pile head can potentially disturb this delicate alignment [8].

To determine whether a hammer blow inflicted plastic deformation at the pile head, a non-collocated method which relies on conventional strain measurement devices has been proposed in [9]. However, this approach requires the sensors to be mounted on the monopile, which makes them prone to damage as a result of energetic hammer blows. Hence, hammer-induced plastic deformation is preferably inferred from data collected by a non-contact sensor. Therefore, this paper focusses on the strain-induced change in the magnetic stray field of the steel pile, since this field permeates the space around the structure allowing for non-contact measurement. The aim of the stray field technique is to detect plastic deformation in an early stage using a non-collocated and non-contact sensor. During pile driving, when a region of plastic deformation is detected, the driving process can be altered to avoid further damage to the pile. Moreover, plastic deformation is detrimental for the service life of the support structure. Hence, by localising and quantifying the damage, the implications for the structural integrity can be determined.

Currently, several magnetic methods exist to detect plastic deformation in steel specimens. The first group of these methods actively

---

* Corresponding author.
 E-mail address: p.c.meijers@tudelft.nl (P.C. Meijers).

employ an external magnetic field during the evaluation process. Plastic deformation is subsequently detected by (i) analysing the characteristics of measured magnetisation curves [10,11], (ii) determining the intensity of the Barkhausen noise [12,13], or (iii) measuring the magnetic stray field when the specimen is magnetically saturated [14,15]. The latter technique has been applied to localise defects in pipelines [16–18] and in wire ropes used in suspension bridges [19]. However, these active methods require the generation of a substantial external magnetic field in the vicinity of the structure. For an offshore monopile installation, actively generating such a field is deemed impractical given the large structural dimensions.

In contrast, passive magnetic methods operate using only the ambient magnetic field, e.g. the geomagnetic field. For lab-scale specimens, stress concentration zones, cracks and regions of plastic deformation have successfully been located [20–22]. However, large-scale cylindrical structures exhibit a substantial demagnetising field due to their geometry [23], complicating the analysis of the magnetic stray field. Thus far, little experimental data for such structures have been reported. Normally, a specimen subjected to a passive magnetic evaluation technique is fully demagnetised before a load is applied to erase the magnetic history, as the presence of an initial magnetisation frustrates the detection of defects [24–26]. For large-scale structures, fully demagnetising the whole structure is practically impossible, as this requires a carefully-controlled external magnetic field on a massive scale.

Passive magnetic methods record the irreversible changes in the magnetic stray field, since a mechanical stress applied to the system, either below or above the material's elastic limit, irreversibly alters its magnetisation [27,28]. To date, all methods used to identify whether an irreversible change in the magnetisation is caused by elastic or plastic strains are developed under well-controlled conditions in which the location of the plastic deformation is known a priori and the loading is introduced gradually [29–31]. However, for large-scale structures this is generally not the case, prohibiting the application of the current methods. In this paper, the irreversible magnetisation change caused by plastic deformation is successfully identified in a steel cylinder subjected to axial impacts without a priori knowledge of the exact circumferential location of the damage by considering the tendency of the stray field to converge to a global magnetic equilibrium. Subsequently, the observed behaviour is simulated by applying a simple empirical model for the structure's magnetic susceptibility.

This paper is structured as follows. Section 2 provides general background regarding the magnetic stray field and the causes for irreversible change in that field. In Section 3, the set-up of the axial-impact experiment is presented, of which the results are discussed in Section 4. Section 5 presents the modelling of the measured evolution of the stray field. Finally, conclusions are drawn in Section 6.

2. Irreversible changes of the magnetic stray field

Surrounding the steel structure shown in Fig. 1a, the total magnetic field $\mathbf{B}_t(\mathbf{p})$ at point $\mathbf{p}$ consists of a uniform background field $\mathbf{B}_0$ and the magnetic stray field of the structure $\mathbf{B}(\mathbf{p})$:

$$\mathbf{B}_t(\mathbf{p}) = \mathbf{B}_0 + \mathbf{B}(\mathbf{p}). \tag{1}$$

The former represents, for instance, the Earth's magnetic field, which—for the current purpose—is assumed space and time invariant. Changes in the latter field, $\mathbf{B}(\mathbf{p})$, are directly related to changes in the total remanent magnetisation of the structure $\mathbf{M}(\mathbf{r})$ since these two quantities are related as follows [32]:

$$\mathbf{B}(\mathbf{p}) = \frac{\mu_0}{4\pi} \int_\Omega \left[\frac{3\,(\mathbf{M}(\mathbf{r}) \cdot \mathbf{s})\,\mathbf{s}}{\|\mathbf{s}\|^5} - \frac{\mathbf{M}(\mathbf{r})}{\|\mathbf{s}\|^3} \right] \, \mathrm{d}\Omega, \tag{2}$$

in which $\mathbf{r}$ is the position vector that characterises all points within the structure's volume Ω, $\mathbf{s} = (\mathbf{p} - \mathbf{r})$ is the separation vector, and μ_0 is the magnetic constant. Consequently, measured changes of $\mathbf{B}_t(\mathbf{p})$

Table 1
Chemical composition of the steel cylinder.

Element	C	Si	Mn	P	S	Cr
%	0.14	0.180	0.79	0.11	0.007	0.17

in between load cycles directly reflect the irreversible changes in the magnetisation, which result from two different physical processes.

First, whenever the strain introduced by a load cycle remains below the elastic limit of the material, the strain energy supplied by the load enables the magnetic domain walls to move towards a magnetic equilibrium by overcoming pinning sites which prevented this movement in the first place [33,34]. Consecutive load cycles of the same magnitude do not irreversibly alter the magnetisation further. However, when a new loading cycle induces strains that surpass the previously endured peak strain, an irreversible change occurs towards a new magnetic equilibrium state [31]. Note that these processes, although related to the elastic regime, may cause irreversible changes in the magnetisation.

Second, as soon as plastic deformation develops in the structure, the dislocation density locally increases [35]. In conjunction, the number of magnetic domain walls increases; since these walls are pinned by the imperfections, the size of the average magnetic domain in the material is effectively reduced. As a consequence, the bulk magnetisation irreversibly decreases for the given external field. Moreover, the plastic deformation introduces residual strains in the material. Both effects resulting from plastic deformation irreversibly change the structure's magnetisation [36]. As a first load cycle that exceeds the material's yield limit simultaneously introduces a new peak strain, both aforementioned irreversible changes of the magnetisation occur in conjunction, obscuring the direct physical process. Here, a method is developed to distinguish between the two causes of permanent changes in the magnetic stray field, which in essence allows one to separate plastic from elastic deformations in the structure.

3. Experimental set-up

To assess whether the above-described two types of irreversible changes can be discriminated when plastic deformation develops in an uncontrolled environment, an axial drop-weight experiment has been conducted on a thin-walled steel cylinder, for which the set-up is presented in Fig. 1a. The length of the cylinder is $L = 1500$ mm; its outer diameter equals $D = 406.4$ mm; and its wall thickness is $h = 2.5$ mm. The steel grade is S275J2H with tensile yield stress of 300 N/mm², ultimate strength of 484 N/mm² and Young's modulus $E = 210$ GPa. Table 1 presents the chemical composition of the material.

A 403 kg concrete mass, which can fall freely along an aluminium guiding system from different heights ℓ, provides the means to introduce an axial impact and thus compressive strain of varying amplitude in the structure. Axial strain gauges (type: UFLA-5-11) located at $z = -200$ mm measure the structure's deformation during impact to quantify these strains, which are recorded using a 16-bit data acquisition system (*National Instruments* USB-6343) and a sampling frequency of 50 kHz. Note that, even though the structure is axially symmetric, an impact does not induce a perfectly axially-symmetric strain state due to the fact that it is practically impossible to assure perfect symmetry of the impact load. Hence, the strain field is expected to have an unknown circumferential distribution. Moreover, the strain gauges are not positioned in the axial plane where plastic deformation is expected to develop. However, the strain gauges are merely used to obtain an indication of magnitude of the impact-induced strains and will not be directly compared to the magnetic stray field measurements.

In between impacts, the magnetic field around the top of the cylinder is measured with a tri-axial fluxgate magnetometer (type: FLC3-70), which has a measuring range of ± 200 μT, a sensitivity of 0.035 μT/mV. The sensor is mounted on a ring which can rotate and be positioned at various heights and offsets relative to the structure. By revolving
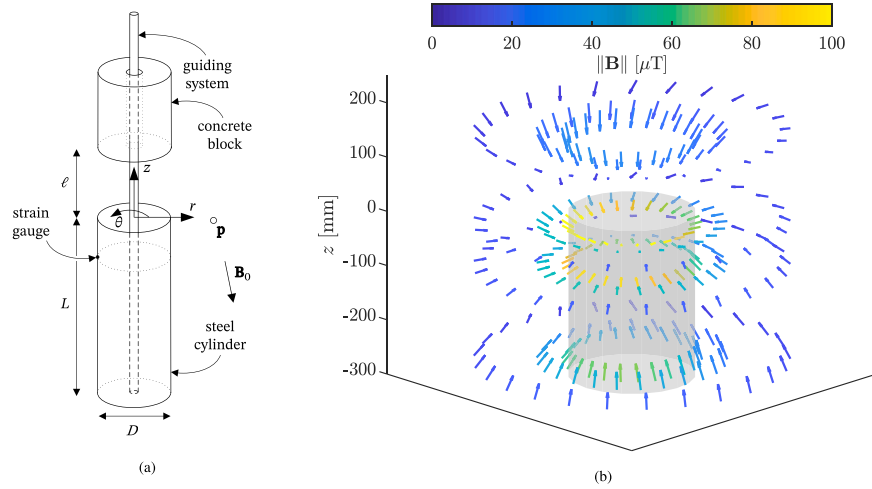
Fig. 1. (a) Schematic of the set-up of the thin-walled cylinder, including the background field $\mathbf{B}_0$. (b) Measured magnetic stray field in the vicinity of the top of the cylinder after five impacts from $\ell = 1000\,\text{mm}$ (test 2e).

Table 2
Detailed description of the tests in consecutive order. Suffixes i, e and p denote initial state, elastic and plastic deformation, respectively. The drop height is represented by ℓ, the (average) measured peak strain is $\delta\varepsilon_z$ and the number of impacts needed to reach a magnetic equilibrium is denoted by #.

id	ℓ [mm]	$\delta\varepsilon_z$ [μm/m]	#
1i	–	–	–
2e	1000	832	5
3e	1500	1200	5
4e	2000	1510	8
5p	2500	1574	1
6p	2500	1550	1
7p	2500	1544	1

the sensor around the cylinder and subsequently applying Eq. (1), a spatial map of the magnetic stray field is identified. During rotation, a data point is recorded every 1.5°, and afterwards the stray field data is presented unfiltered. As an example, Fig. 1b shows the stray field close to the top of the cylinder measured after five impacts from a drop height of 1000 mm (test 2e). As the field lines converge towards the top of the cylinder, this end acts as an effective magnetic south pole; given the fact that the magnetic stray field is divergence free, the lower end of the cylinder serves as the effective north pole (not shown in the figure).

To eliminate the influence of the magnetothermomechanical history of the cylinder, the structure is initially demagnetised using a hand-held degaussing device. Nevertheless, due to the presence of the external field, the magnetisation will not be completely reduced to zero. The effect of this imperfect demagnetisation on the validity of the results and the proposed method for plasticity detection is addressed later in the discussion of the experimental results. After the demagnetisation, the structure is subjected to an axial impact, which is repeated until a magnetic equilibrium is reached, i.e. the remanent magnetic stray field no longer changes. After mapping the stray field, the drop height is increased. This procedure is repeated until visible plastic deformation starts to develop.

4. Experimental results and discussion

An overview of the set of experiments is shown in Table 2, including the measured peak strain $\delta\varepsilon_z$ and the number of impacts needed to reach a magnetic equilibrium. The tests are numbered in consecutive order and have suffixes i, e and p to denote initial state, elastic and plastic deformation, respectively. Rather than depicting the three-dimensional field as presented in Fig. 1b, Fig. 2 focuses on the dominant component of the stray field; the radial component B_r. In accordance

with other low-velocity drop-weight experiments [37], it is expected that plastic deformation will develop close to the impacted end. Hence, Fig. 2 shows the data measured on a ring at $z = -20\,\text{mm}$ and $r = 223.2\,\text{mm}$, i.e. at 20 mm from the cylinder's surface. In the circumferential profile, Fig. 2a, four distinct regions are shaded, indicating the positions and time moments at which visual plastic deformation developed. Figs. 2a and 2c show the plastically deformed surface after test 7p and 5p, respectively. At each region, the evolution of B_r with each test is presented in Fig. 2d, in which the error bars indicate the uncertainty in the measured value corresponding to 2% of $\|\mathbf{B}\|$.

Initially (test 1i), the structure is close to the demagnetised state due to the partial demagnetisation procedure. Nonetheless, since the external geomagnetic field is not controlled in the set-up, the magnetisation in the sample still adheres to some extent to the direction of this external field, which results in the measured inhomogeneous initial stray field profile of B_r. The observed skewness of the initial (and subsequent) profiles results from the geometry-induced demagnetising field caused by the transverse component of the geomagnetic field, which points approximately towards $\theta = 325°$.

Subsequently, the axial impacts introduce sufficient energy to magnetise the structure further; its magnetisation aligns with the external field $\mathbf{B}_0$. As this field has a predominate downward component, it drives the magnetisation vector towards the negative z-axis, resulting in the observed direction of B_r towards the top of the cylinder. This alignment, nevertheless, is not perfect due to the obstructing effect of internal pinning sites. Each impact supplies strain energy to the structure, which causes some domain walls to break away from these pinning site and settle on a stronger pinning site, resulting in an irreversible change in the structure's magnetisation. After a few impacts from the same impact height, the domain configuration no longer changes, i.e. the magnetisation has reached a metastable equilibrium. When a larger amount of strain energy is provided to the system, e.g. by increasing the impact height, this additional energy allows some domain walls to overcome their pinning site and settle into another configuration, which represents a new metastable equilibrium. Fig. 3 shows the evolution of the radial component of the stray field including the intermediate values after the impacts that comprise the first three tests, displaying this convergence to an equilibrium value with repetition of the load. Similar behaviour under elastic loads has previously been reported [31].

The large difference between the initial state (1i) and the stray field after 5 impacts of 1000 mm (2e) stems from the fact that the initial state is close of the demagnetised state, in which the magnetic domains are oriented more or less randomly. Due to the energy supplied to the material by the impacts, the magnetic domain walls are reordered such that
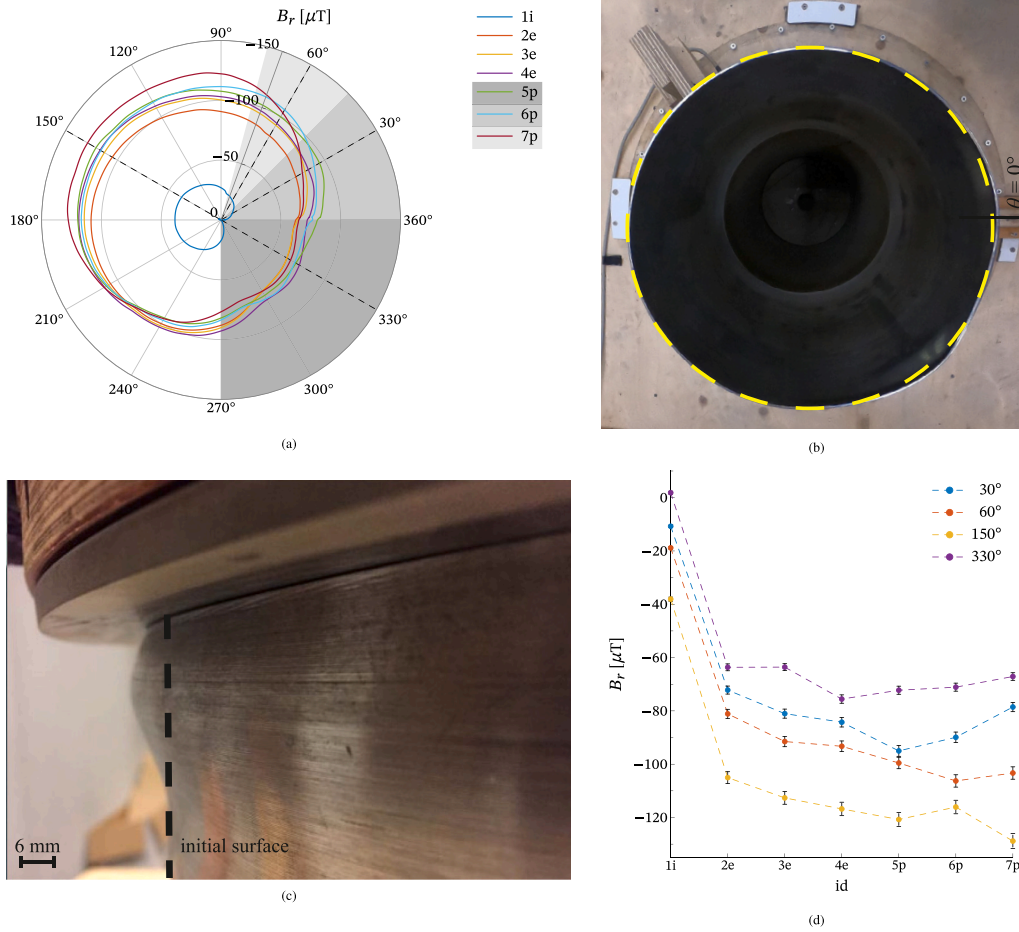
Fig. 2. (a) Circumferential profile of the radial component of the magnetic stray field B_r measured at $z = -20$ mm and $r = 223.2$ mm, which is an offset of 20 mm from the cylinder's surface. Grey areas indicate regions where visible plastic deformation developed; darker shaded regions were inflicted earlier. (b) Top view of the deformed cylinder after test 7p. The yellow dashed line indicates the position of the initial surface of the cylinder. (c) Plastic deformation at the top of the cylinder after test 5p. (d) Evolution of B_r in between tests along four selected circumferential positions.

the overall magnetisation of the structures aligns better to the external magnetic field. For the subsequent tests within the elastic regime, the differences between successive stray field values are noticeably smaller, since the domain wall configuration is already much closer to the global equilibrium state. Nonetheless, the observed evolution of the stray field is still significantly larger than the measurement error. An exception to this trend appears between 2e and 3e at $\theta = 330°$ (Fig. 2d). However, this difference lies within the error margin; hence, the converging trend appears to continue as well.

In contrast, as soon as plastic deformation develops, e.g. test 5p at $\theta = 330°$, the direction of the change in the stray field deviates from this trend. This behaviour is a consequence of the increased pinning site density, leading to a decrease in the bulk magnetisation. For circumferential positions where no visible damage developed in test 5p ($\theta = 30°$, $\theta = 60°$ and $\theta = 150°$), the trend towards global equilibrium simply continues until plastic deformation does develop, i.e. during test 6p and 7p at $\theta = 30°$ and $\theta = 60°$, respectively. Therefore, it seems that the departure from this trend permits not only detecting, but also localising the damage.

During the development of plastic deformation, the remanent stray field irreversibly changes as a result of three physical processes of which the effects are superimposed:

(i) deterioration of magnetic properties due to the formation of plastic deformation. This always results in a local decrease of strength of the magnetisation, and reciprocally a demise of the stray field's amplitude in the vicinity of the damage;
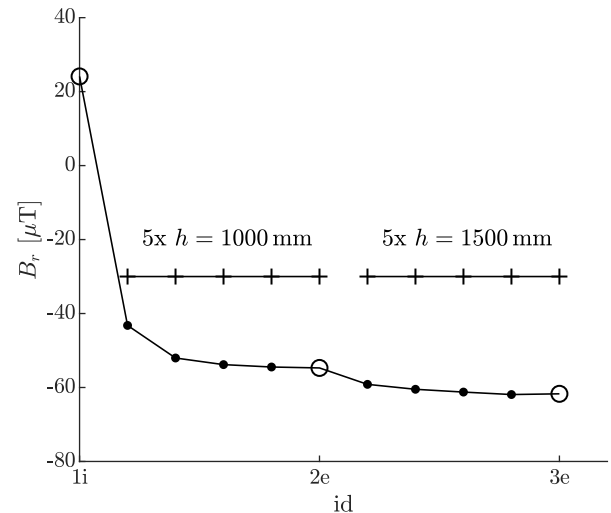

Fig. 3. Measured evolution of the radial component of the remanent stray field at $z = -200$ mm, $r = 223.2$ mm and $\theta = 120°$ for the first three tests showing the intermediate values after each impact.

(ii) irreversible domain wall motion due to energy provided by elastic deformation (Fig. 3). For the presented results, this leads to a relatively small increase of the magnitude of the magnetisation,
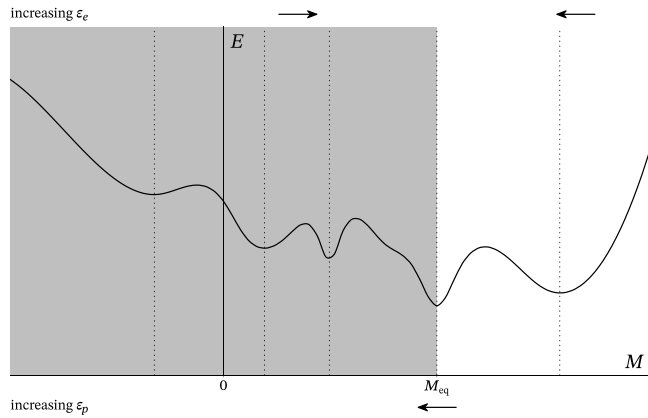
Fig. 4. Simplified representation of the energy E associated with the attained magnetisation M, in which M_{eq} denotes the global magnetic equilibrium.

which is clear from the evolution of the stray field during tests 2e to 4e;

(iii) permanent change in the geometry due to the damage, which brings the surface of the cylinder closer to the sensor (see the inset in Fig. 2a). Normally, the strength of the measured stray field increases when a ferromagnetic material comes closer to a magnetic field sensor.

Of these three processes, only the first reduces the stray field's magnitude. The latter two increase the measured strength of the stray field. Given that, due to the development of the plastic zone, the amplitude of the measured stray field still diminished, one is inclined to conclude that the sustained damage significantly reduced the local magnetisation, and that this decline can only be attributed to the development of a region of substantial plastic deformation.

Although the magnetisation's tendency towards a global equilibrium state resulting from elastic load cycles is pronounced, the experimental data show that the exact value of this magnetic equilibrium state cannot easily be determined a priori. Fortunately, an exact value is unnecessary to detect and localise plastic deformation, since the development of permanent strain violates the described trend. However, for some initial magnetic states, this transgression is not observed when plastic deformation forms. This becomes apparent by a closer examination of a simplified representation of the energy E associated with each value of the structure's magnetisation M (Fig. 4). In reality, the presented line is a hypersurface, which depends on a plethora of parameters: external field strength and orientation, elastic strains, temperature, and, most importantly, the distribution of pinning sites for the magnetic domain walls. The (local) minima of the hypersurface, indicated by the vertical dotted lines, denote the admissible values for the structure's magnetisation.

Assuming that the dislocation distribution does not change significantly due to the induced elastic strains, the additional strain energy introduced by a new peak strain provides the system with sufficient energy to overcome the barrier that originally prevented it from reaching a lower energy state. Hence, induced elastic strains ε_e move the magnetisation closer to the global equilibrium M_{eq}, which is illustrated by the arrows at the top of Fig. 4. When plastic strain ε_p develops, the dislocation density increases. These newly-formed pinning sites disintegrate the existing magnetic domains, reshaping the hypersurface, and shifting the global minimum towards zero magnetisation. The direction of the magnetisation change caused by plastic deformation is marked by the arrow below the figure.

When the structure's initial magnetic state is in the grey-shaded area shown in Fig. 4, the remanent stray field displays the behaviour described above: the deviation from the trend allows one to discriminate between the two causes for irreversible magnetisation changes.

Nonetheless, for an initial magnetisation in the unshaded area, both elastic and plastic strain tend to decrease the magnetisation, obscuring the cause of the permanent shift in the magnetisation. Hence, to successfully identify the source of an irreversible magnetisation change, the initial magnetic state of the structure must lie within the shaded area. This specific initial state can be achieved by simply demagnetising the area of interest. As seen from the presented experimental data, perfect demagnetisation is not required.

5. Modelling the irreversible stray field changes

Based on the presented results, quantifying the plastic deformation is, at present, not yet possible. However, by including a dependency on plastic strain in a model for the magnetisation $\mathbf{M}(\mathbf{r})$ in Eq. (2), this should ultimately be feasible. In the following, the stray field of the cylinder is simulated using a rudimentary model for the magnetic susceptibility to ascertain whether such a model is able to replicate the observed irreversible stray field changes under elastic and plastic deformation.

5.1. The stray field in the presence of an external field

Even though the external field $\mathbf{B}_0$ is assumed to be time and space invariant, the magnetisation of the cylinder will not be uniform due to the geometry of the structure, which leads to a significant demagnetising field [38]. To compute the magnetic field generated by the structure's magnetisation, a numerical approach applicable to steel sheets is adopted [32], which assumes that the magnetisation component in the normal direction of the sheet (the radial component M_r in the current situation) is negligible.

By evenly subdividing the pile's volume Ω into N_θ elements in the circumferential and N_z elements in the axial direction, the structure is discretised, and the total number of elements equals $N = N_\theta N_z$. Under the assumption that the magnetisation is constant over each element and is concentrated at the element's barycentre $\mathbf{r}_i$, i.e. $\mathbf{M}(\mathbf{r}_i)$, the magnetic field at $\mathbf{p}$ is given by a summation of the contributions from all elements:

$$\mathbf{B}(\mathbf{p}) = \frac{\mu_0}{4\pi} \sum_{i=1}^{N} \oint_{\Gamma_i} \mathbf{M}(\mathbf{r}_i) \cdot \mathbf{n}_i \frac{\mathbf{p} - \mathbf{r}_i}{\|\mathbf{p} - \mathbf{r}_i\|^3} \, d\Gamma_i, \tag{3}$$

in which μ_0 denotes the magnetic constant, and $\mathbf{n}_i$ is the outward normal to the element's boundary Γ_i. Note that Eq. (3) is simply the discretised counterpart of the continuous function given by Eq. (2). By evaluating the integrals, the expression above is rewritten as follows:

$$\mathbf{B}(\mathbf{p}) = \mu_0 \sum_{i=1}^{N} \mathbf{G}_i \mathbf{M}(\mathbf{r}_i) = \mu_0 \mathbf{G}_\mathbf{p} \mathbf{M}, \tag{4}$$

in which $\mathbf{G}_i$ contains the values of the evaluated integrals at each element. In the latter part of the expression, these contributions are condensed into a single matrix $\mathbf{G}_\mathbf{p}$, and $\mathbf{M}$ is a vector incorporating the magnetisation components from all elements. Since the radial magnetisation component is deemed insignificant, $\mathbf{M}$ contains $2N$ entries.

To express the magnetisation in terms of the external magnetic field $\mathbf{B}_0$, an appropriate constitutive equation is required. For a (locally) isotropic material, a scalar magnetic susceptibility χ suffices. Hence, the following implicit constitutive equation is employed:

$$\mathbf{M} = \chi \left(\frac{\mathbf{B}_0}{\mu_0} + \mathbf{G}_\mathbf{r} \mathbf{M} \right), \tag{5}$$

in which $\mathbf{G}_\mathbf{r}$ is a $2N \times 2N$ matrix representing the non-local interaction of the structure's magnetisation, which is obtained by substituting $\mathbf{p} = \mathbf{r}_i$ for each element in Eq. (4). Assuming that χ is not a function of the magnetisation itself, rearrangement of Eq. (5) yields

$$\mathbf{M} = \chi \left(\mathbf{I} - \chi \mathbf{G}_\mathbf{r} \right)^{-1} \frac{\mathbf{B}_0}{\mu_0}, \tag{6}$$

Parameter	Value
D	406.4 mm
L	1500 mm
h	2.5 mm
N_θ	64
N_z	80

in which **I** is the $2N \times 2N$ identity matrix and $(\cdot)^{-1}$ denotes a matrix inversion. When the susceptibility in known, the structure's magnetisation is computed by means of Eq. (6); subsequently, the stray field at **p** is determined by employing Eq. (4).

5.2. Model for the magnetic susceptibility

The model for the magnetic susceptibility should reflect the observations mentioned in the discussion above. To accommodate these, the following empirical expression for the magnetic susceptibility χ is proposed:

$$\chi\left(\theta, z, \delta\varepsilon_z, \varepsilon_p\right) = \chi_0 + \alpha_e \left\|\delta\varepsilon_z(\theta, z)\right\| - \alpha_p \left\|\varepsilon_p(\theta, z)\right\| \tag{7}$$

in which χ_0 denotes the susceptibility in the partially demagnetised initial state and $\|\cdot\|$ represents the absolute value. The term $\alpha_e \left\|\delta\varepsilon_z(\theta, z)\right\|$ reflects the tendency of the magnetisation to converge towards a metastable magnetic equilibrium whenever a new peak strain $\delta\varepsilon_z$ is sustained, with α_e a positive real-valued constant. Since the magnetic properties of the material deteriorate with increasing plastic deformation, the term $-\alpha_p \left\|\varepsilon_p(\theta, z)\right\|$ is added to the model, in which α_p is positive model constant. More advanced empirical models for the inclusion of the effect of plastic deformation have been proposed in literature [36,39]; however, effectively, these models simply reduce the susceptibility with increasing plastic deformation. Hence, the basic form given by Eq. (7) is adopted in this paper.

Although the definition of a magnetic susceptibility is common in the treatment of magnetoelastic problems [40,41], these normally do not account for time-dependent irreversible changes of the magnetic properties. As the latter are essential for the description of the evolution of the magnetisation caused by repeated impacts, the formulation of χ in Eq. (7) implicitly includes the mechanical loading history via $\delta\varepsilon_z$ and ε_p.

Naturally, the proposed model for χ is a function of the spatial coordinates, as the plastic deformations develops in certain confined regions. Fig. 5a presents the applied susceptibility at the four circumferential positions which are identical to the locations in Fig. 2. Since it is assumed that almost the entirety of the structure remains in the elastic regime, the susceptibility is a monotonic function that increases with increasing drop height. The corresponding values are represented by the line for $\theta = 150°$ (Fig. 5a). At the other three locations, plastic deformation does develop; and it is assumed that this damage is confined to a small region close to the top of the cylinder, i.e. between $0 \geq z \geq -50$ mm. The circumferential location of the damage corresponds to the grey-shaded areas in Fig. 2a. To complete the model description, the external field $\mathbf{B}_0 = [B_0^x \; B_0^y \; B_0^z]^T = [14.3 \; -9.5 \; -35.3]^T \mu$T, and the numerical values for the remaining relevant parameters are listed in Table 3.

Fig. 5b presents the computed evolution of the radial component of the stray field B_r at $z = -20$ mm, $r = 223.2$ mm and the four circumferential positions. Apart from the initial state (1i), the correspondence between the simulation and the measurements is excellent. The discrepancy for the initial state could be attributed to intricate magnetic behaviour close the demagnetised state, which cannot be captured by a uniform isotropic magnetic susceptibility. On the contrary, the scalar susceptibility is sufficient to model the observed evolution of the stray field for areas that remain in the elastic regime (e.g. 2e to 6p at $\theta = 60°$). Moreover, the deviation of the trend is captured by the localised decrease of χ due to the development of plastic deformation. Of course, currently, numerical values for the modelled susceptibility are calibrated to fit the measurement data, since the exact amount of plastic deformation is initially unknown; the total strain was not measured at the actual location were that damage occurred. However, the fact that the stray field's evolution can be simulated using such an elementary isotropic model seems to show that the processes discussed in Section 4 govern the observed irreversible magnetisation changes. The proposed modelling approach provides a promising starting point for further research into the application of the described observation to identify, localise and potentially quantify regions of plastic deformation as a result of repeated impact loads.

6. Conclusions

Magnetic stray field measurements of a steel cylinder subjected to axial impacts from various heights demonstrate that irreversible changes in the structure's magnetisation caused by plastic deformation can be distinguished from irreversible changes due to elastic deformation. The former changes result in a deviation from the tendency of the magnetisation to converge towards a global equilibrium when the structure is initially close to the demagnetised state. These results are obtained in an experiment in which the exact location of the plastic deformation is unknown a priori and the loading is not well-controlled. With the aid of an empirical isotropic model for the structure's magnetic susceptibility, the measured data is successfully reproduced. The approach based on evolution of the structure's magnetic stray field presented in this paper is able to detect, localise, and potentially quantify regions of plastic deformation in dynamically loaded large-scale structures.

CRediT authorship contribution statement

P.C. Meijers: Conceptualization, Methodology, Software, Validation, Formal analysis, Investigation, Writing – original draft, Visualisation, Data curation. **C.T. Jolink:** Conceptualization, Methodology, Investigation, Writing – original draft. **A. Tsouvalas:** Conceptualization, Writing – review & editing, Supervision. **A.V. Metrikine:** Conceptualization, Writing – review & editing, Supervision.

Declaration of competing interest

The authors declare that they have no known competing financial interests or personal relationships that could have appeared to influence the work reported in this paper.
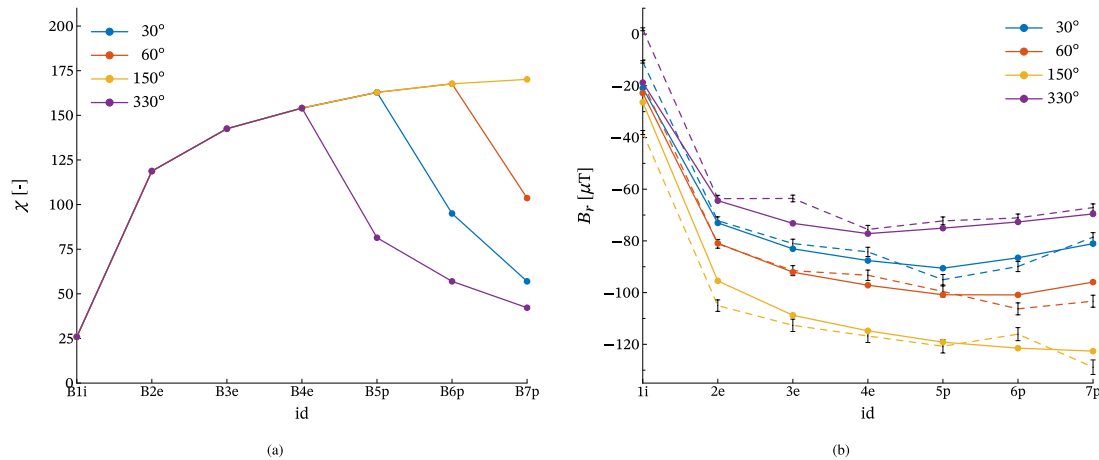
Fig. 5. (a) Modelled magnetic susceptibility χ in the four regions. (b) Simulated evolution of B_r using the proposed model for χ. As a reference, the dashed lines present the measured evolution of B_r.

References

[1] Perveen R, Kishor N, Mohanty SR. Off-shore wind farm development: Present status and challenges. Renew Sustain Energy Rev 2014;29:780–92. http://dx.doi.org/10.1016/j.rser.2013.08.108.

[2] WindEurope, Offshore Wind in Europe. Key trends and statistics 2019. Tech. rep., WindEurope; 2020.

[3] Doherty P, Gavin K. Laterally loaded monopile design for offshore wind farms. Proc Inst Civ Eng - Energy 2012;165(1):7–17. http://dx.doi.org/10.1680/ener.11.00003.

[4] Jensen KS, r. J. Petersen S, Pedersen RR. European offshore wind engineering–past, present and future. Proc Inst Civ Eng - Civ Eng 2018;171(4):159–65. http://dx.doi.org/10.1680/jcien.17.00040.

[5] Chen T, Wang X, Gu X, Zhao Q, Yuan G, Liu J. Axial compression tests of grouted connections in jacket and monopile offshore wind turbine structures. Eng Struct 2019;196:109330. http://dx.doi.org/10.1016/j.engstruct.2019.109330.

[6] Dallyn P, El-Hamalawi A, Palmeri A, Knight R. Experimental investigation on the development of wear in grouted connections for offshore wind turbine generators. Eng Struct 2016;113:89–102. http://dx.doi.org/10.1016/j.engstruct.2015.11.028.

[7] Gollub P, Jensen JF, Giese D, Güres S. Flanged foundation connection of the Offshore Wind Farm Amrumbank West - Concept, approval, design, tests and installation: Flanged foundation connection of the Offshore Wind Farm Amrumbank West - Concept, approval, design, tests and installation. Stahlbau 2014;83(8):522–8. http://dx.doi.org/10.1002/stab.201410178.

[8] Janele TO, Landskröner S, Klose M. Berechnung der Rammschädigung an Flanschen von Monopile-Gründungen. Stahlbau 2015;84(7):494–500. http://dx.doi.org/10.1002/stab.201510283.

[9] Meijers PC, Tsouvalas A, Metrikine AV. A non-collocated method to quantify plastic deformation caused by impact pile driving. Int J Mech Sci 2018;148:1–8. http://dx.doi.org/10.1016/j.ijmecsci.2018.08.013.

[10] Makar JM, Atherton DL. Effect of uniaxial stress on the reversible and irreversible permeabilities of 2% Mn pipeline steel. IEEE Trans Magn 1994;30(4):1380–7. http://dx.doi.org/10.1109/20.305536.

[11] Takahashi S, Kobayashi S, Tomáš I, Dupre L, Vértesy G. Comparison of magnetic nondestructive methods applied for inspection of steel degradation. NDT & E Int 2017;91:54–60. http://dx.doi.org/10.1016/j.ndteint.2017.06.001.

[12] Maylin MG, Squire PT. The effects of stress on induction, differential permeability and Barkhausen count in a ferromagnet. IEEE Trans Magn 1993;29(6):3499–501. http://dx.doi.org/10.1109/20.281209.

[13] Kleber X, Vincent A. On the role of residual internal stresses and dislocations on Barkhausen noise in plastically deformed steel. NDT & E Int 2004;37(6):439–45. http://dx.doi.org/10.1016/j.ndteint.2003.11.008.

[14] Wang Y, Liu X, Wu B, Xiao J, Wu D, He C. Dipole modeling of stress-dependent magnetic flux leakage. NDT & E Int 2018;95:1–8. http://dx.doi.org/10.1016/j.ndteint.2018.01.004.

[15] Babbar V, Bryne J, Clapham L. Mechanical damage detection using magnetic flux leakage tools: Modeling the effect of dent geometry and stresses. NDT & E Int 2005;38(6):471–7. http://dx.doi.org/10.1016/j.ndteint.2004.12.002.

[16] Atherton DL, Teitsma A. Detection of anomalous stresses in gas pipelines by magnetometer survey (invited). J Appl Phys 1982;53(11):8130–5. http://dx.doi.org/10.1063/1.330316.

[17] Li Z, Jarvis R, Nagy PB, Dixon S, Cawley P. Experimental and simulation methods to study the Magnetic Tomography Method (MTM) for pipe defect detection. NDT & E Int 2017;92:59–66. http://dx.doi.org/10.1016/j.ndteint.2017.07.018.

[18] Ege Y, Coramik M. A new measurement system using magnetic flux leakage method in pipeline inspection. Measurement 2018;123:163–74. http://dx.doi.org/10.1016/j.measurement.2018.03.064.

[19] Christen R, Bergamini A, Motavalli M. Influence of steel wrapping on magneto-inductive testing of the main cables of suspension bridges. NDT & E Int 2009;42(1):22–7. http://dx.doi.org/10.1016/j.ndteint.2008.08.003.

[20] Bao S, Jin P, Zhao Z, Fu M. A review of the metal magnetic memory method. J Nondestruct Eval 2020;39(1):11. http://dx.doi.org/10.1007/s10921-020-0652-z.

[21] Dong L, Xu B, Dong S, Song L, Chen Q, Wang D. Stress dependence of the spontaneous stray field signals of ferromagnetic steel. NDT & E Int 2009;42(4):323–7. http://dx.doi.org/10.1016/j.ndteint.2008.12.005.

[22] Wang ZD, Gu Y, Wang YS. A review of three magnetic NDT technologies. J Magn Magn Mater 2012;324(4):382–8. http://dx.doi.org/10.1016/j.jmmm.2011.08.048.

[23] Viana A, Rouve L-L, Cauffet G, Coulomb J-L. Magneto-mechanical effects under low fields and high stresses - application to a ferromagnetic cylinder under pressure in a vertical field. IEEE Trans Magn 2010;46(8):2872–5. http://dx.doi.org/10.1109/TMAG.2010.2043825.

[24] Guo P, Chen X, Guan W, Cheng H, Jiang H. Effect of tensile stress on the variation of magnetic field of low-alloy steel. J Magn Magn Mater 2011;323(20):2474–7. http://dx.doi.org/10.1016/j.jmmm.2011.05.015.

[25] Leng J, Xu M, Zhou G, Wu Z. Effect of initial remanent states on the variation of magnetic memory signals. NDT & E Int 2012;52(Supplement C):23–7. http://dx.doi.org/10.1016/j.ndteint.2012.08.009.

[26] Ren S, Ren X, Duan Z, Fu Y. Studies on influences of initial magnetization state on metal magnetic memory signal. NDT & E Int 2019;103:77–83. http://dx.doi.org/10.1016/j.ndteint.2019.02.002.

[27] Brown WF. Irreversible magnetic effects of stress. Phys Rev 1949;75(1):147–54. http://dx.doi.org/10.1103/PhysRev.75.147.

[28] Jiles DC, Atherton DL. Theory of the magnetisation process in ferromagnets and its application to the magnetomechanical effect. J Phys D: Appl Phys 1984;17(6):1265. http://dx.doi.org/10.1088/0022-3727/17/6/023.

[29] Yao K, Wang ZD, Deng B, Shen K. Experimental research on metal magnetic memory method. Exp Mech 2012;52(3):305–14. http://dx.doi.org/10.1007/s11340-011-9490-3.

[30] Leng J, Liu Y, Zhou G, Gao Y. Metal magnetic memory signal response to plastic deformation of low carbon steel. NDT & E Int 2013;55(Supplement C):42–6. http://dx.doi.org/10.1016/j.ndteint.2013.01.005.

[31] Li Z, Dixon S, Cawley P, Jarvis R, Nagy PB, Cabeza S. Experimental studies of the magneto-mechanical memory (MMM) technique using permanently installed magnetic sensor arrays. NDT & E Int 2017;92(Supplement C):136–48. http://dx.doi.org/10.1016/j.ndteint.2017.07.019.

[32] Chadebec O, Coulomb J-L, Janet F. A review of magnetostatic moment method. IEEE Trans Magn 2006;42(4):515–20. http://dx.doi.org/10.1109/TMAG.2006.870929.

[33] Atherton D, Welbourn C, Jiles D, Reynolds L, Scott-Thomas J. Stress-induced magnetization changes of steel pipes–Laboratory tests, Part II. IEEE Trans Magn 1984;20(6):2129–36. http://dx.doi.org/10.1109/TMAG.1984.1063572.

[34] Makar JM, Atherton DL. Effects of isofield uniaxial cyclic stress on the magnetization of 2% Mn pipeline steel - behavior on minor hysteresis loops and small major hysteresis loops. IEEE Trans Magn 1995;31(3):2220–7. http://dx.doi.org/10.1109/20.376241.

[35] Gilman JJ. Microdynamical theory of plasticity. In: McMahon CJ, editor. Advances in materials research, Vol. 2. New York: Interscience Publishers; 1968.

[36] Sablik MJ, Yonamine T, Landgraf FJG. Modeling plastic deformation effects in steel on hysteresis loops with the same maximum flux density. IEEE Trans Magn 2004;40(5):3219–26. http://dx.doi.org/10.1109/TMAG.2004.832763.

[37] Karagiozova D, Jones N. Dynamic elastic–plastic buckling of circular cylindrical shells under axial impact. Int J Solids Struct 2000;37(14):2005–34. http://dx.doi.org/10.1016/S0020-7683(98)00343-6.

[38] Beleggia M, Vokoun D, De Graef M. Demagnetization factors for cylindrical shells and related shapes. J Magn Magn Mater 2009;321(9):1306–15. http://dx.doi.org/10.1016/j.jmmm.2008.11.046.

[39] Wang ZD, Deng B, Yao K. Physical model of plastic deformation on magnetization in ferromagnetic materials. J Appl Phys 2011;109(8):083928. http://dx.doi.org/10.1063/1.3574923.

[40] Liu LL, Feng WJ, Ma P. A penny-shaped magnetically dielectric crack in a magnetoelectroelastic cylinder under magnetoelectromechanical loads. ZAMM - J Appl Math Mech / Z Angew Math Mech 2015;(2):12.

[41] Khurshudyan AZ. Min(max)imization of horizontal and vertical displacements of a fibre-reinforced magneto-elastic cantilever rod. ZAMM - J Appl Math Mech / Z Angew Math Mech 2018;98(11):1924–9. http://dx.doi.org/10.1002/zamm.201800192.